

some LMXBs shine intermittently²⁸, the number of active sources at any time among ten or twenty LMXBs is not likely to fluctuate by more than a few. Therefore, we do not expect that the central X-ray source in M33 varies by more than a few tens per cent.

In addition to LMXBs, we expect that millisecond pulsars also will be formed more readily than in galactic globular clusters. More than twenty have so far been discovered in globular clusters. Searches are still far from complete. Therefore, an order-of-magnitude estimate for the population of such pulsars in the M33 nucleus is ~ 100 , which would make it even more extreme than the galactic globular 47 Tucanae, which contains at least 11 millisecond pulsars²⁹. Detections of individual pulsars in M33 are not feasible at present. The total radio emission from ~ 100 pulsars, which would be concentrated in the inner 0.1", may, however, be observable. If a central radio source were discovered in M33, the shape of its spectrum might indicate whether or not it is a collection of pulsars.

The high central density will lead to capture of white dwarf stars as well as of neutron stars. The enhancement with respect to globular clusters will be less marked for the former than for the latter, because white dwarfs do not generally receive a large velocity kick at birth, and are therefore likely to be retained even in globular clusters. But the high central density in M33 may cause cataclysmic binaries to form at a considerably higher rate than in even a highly concentrated globular cluster. Some of these will become recurrent novae. It is difficult to estimate the resulting total nova rate theoretically, but there have been a few novae seen in or near globular clusters over the past 100 years (see ref. 30 and references therein). The true nova rate in globulars may be higher. Therefore, a rough guess for the nova rate in the nucleus of M33 is ~ 1 event per century.

Finally, blue stragglers will form through mergers caused by physical collisions of stars in the dense centre of the nucleus, where interstellar distances are only ~ 0.005 pc ($\sim 1,000$ AU). As with cataclysmic variables, the enhancement compared with dense globular cluster cores will be modest. Even an optimistic estimate implies that $\leq 10\%$ of the stars in the core of the nucleus are merger remnants. As the total mass of the nucleus is at least an order of magnitude larger than the core mass, we do not expect blue stragglers to constitute more than $\sim 1\%$ of the nucleus. The total mass fraction of blue stragglers needed to explain the anomalous blue colour of the nucleus is $\sim 10\%$. Therefore, we join previous authors in rejecting the interesting possibility that the nucleus is composed of a globular-cluster-type old population. Some star formation must have occurred recently^{1,2,31-34}.

The presence of a small admixture of younger stars should not significantly modify our simple picture of the dynamical evolution of the nucleus. With such a small central relaxation time, all but the youngest stars will have reached local dynamical equilibrium. There is no indication that other complications, such as the presence of gas and dust in the nucleus, have an important role: the nearest H II regions are well outside the nucleus. Of course, past episodes of star formation may have changed the rate of dynamical evolution, possibly speeding core collapse. Also, young stars more massive than $1 M_{\odot}$ will slightly increase the dynamical effects of mass segregation. The situation is not, however, radically different from that of dense globular cluster cores, where physical collisions must have produced numerous merger products (possibly blue stragglers) as a result of physical collisions between stars. Thus, a relatively small fraction of young stars is unlikely to make a marked difference to our order-of-magnitude estimates.

We conclude that core collapse has probably taken place in the nucleus of M33. This may have created the anomalous central X-ray source by producing 10 or more low-mass X-ray binaries. In many ways, M33 may turn out to be an ideal laboratory for studying dynamical processes in star clusters: it is intermediate in properties between the densest galactic nuclei and the densest

globular cluster cores, and it is unusually inactive for a galactic nucleus. □

Received 1 August; accepted 8 October 1991.

- Kormendy, J. Pap. presented at 1990 Aspen Workshop on Stellar Dynamics and Galaxy Formation (1990).
- Kormendy, J. & McClure, R. D. *Astrophys. J.* (submitted).
- Lauer, T. R. *Astrophys. J.* **292**, 104-121 (1985).
- Kormendy, J. *Astrophys. J.* **295**, 73-79 (1985).
- Kormendy, J. in *Nearly Normal Galaxies: From the Planck Time to the Present* (ed. Faber, S. M.) 163-174 (Springer, New York, 1987).
- Tonry, J. L. *Astrophys. J.* **322**, 632-642 (1987).
- Dressler, A. & Richstone, D. O. *Astrophys. J.* **324**, 701-713 (1988).
- Kormendy, J. *Astrophys. J.* **325**, 128-141 (1988).
- Kormendy, J. *Astrophys. J.* **335**, 40-56 (1988).
- Kormendy, J. & Richstone, D. *Astrophys. J.* (submitted).
- Lauer, T. R. *et al. Astrophys. J.* **369**, L41-44 (1991).
- Binney, J. & Tremaine, S. *Galactic Dynamics* (Princeton University Press, 1987).
- Spitzer, L. *Dynamical Evolution of Globular Clusters* (Princeton University Press, 1987).
- Murphy, B., Cohn, H. & Hut, P. *Mon. Not. R. astr. Soc.* **245**, 335-349 (1990).
- Goodman, J. & Hut, P. *Nature* **339**, 40-42 (1989).
- McMillan, S., Hut, P. & Makino, J. *Astrophys. J.* **362**, 522-537 (1990), **372**, 111-124 (1991).
- Gao, B., Goodman, J., Cohn, H. & Murphy, B. *Astrophys. J.* **370**, 567-582 (1991).
- Lauer, T. R. *et al. Astrophys. J.* **369**, L45-49 (1991).
- Fabian, A. C., Pringle, J. E. & Rees, M. J. *Mon. Not. R. astr. Soc.* **172**, 15-18P (1975).
- Lee, H. M. & Ostriker, J. P. *Astrophys. J.* **310**, 176-188 (1986).
- Verbunt, F. & Hut, P. in *IAU Symp. 125, The Origin and Evolution of Neutron Stars* (eds Helfand, D. J. & Huang, J. H.) 187-197 (Reidel, Dordrecht, 1987).
- Long, K. S., D'Odorico, S., Charles, P. A. & Dopita, M. A. *Astrophys. J.* **246**, L61-64 (1981).
- Markert, T. H. & Rallis, A. D. *Astrophys. J.* **275**, 571-577 (1983).
- Peres, G., Reale, F., Collura, A. & Fabbiano, G. *Astrophys. J.* **336**, 140-151 (1989).
- Gottwald, M., Pietsch, W. & Hasinger, G. *Astr. Astrophys.* **175**, 45-49 (1987).
- Verbunt, F., van Paradijs, J. & Elson, R. *Mon. Not. R. astr. Soc.* **210**, 899-914 (1984).
- Helfand, D. *Publ. astr. Soc. Pacific* **96**, 913-931 (1984).
- Lewin, P. C. & Joss, W. H. G. *Space Sci. Rev.* **28**, 3-87 (1981).
- Manchester, R. N. *et al. Nature* **352**, 219-221 (1991).
- Hut, P. & Verbunt, F. *Nature* **301**, 587-589 (1983).
- Gallagher, J. S., Goad, J. W. & Mould, J. *Astrophys. J.* **263**, 101-107 (1982).
- Nieto, J.-L. & Auriere, M. *Astr. Astrophys.* **108**, 334-338 (1982).
- O'Connell, R. W. *Astrophys. J.* **267**, 80-92 (1983).
- van den Bergh, S. *Publ. astr. Soc. Pacific* **103** (in the press).

ACKNOWLEDGEMENTS. We thank J. Goodman for discussions and comments about the manuscript and we thank the Aspen Centre for Physics for their hospitality. This work was supported in part by the Alfred P. Sloan Foundation, NASA, the NSF and the California Space Institute.

Structural studies of membranes and surface layers up to 1,000 Å thick using X-ray standing waves

Jin Wang*, Michael J. Bedzyk†‡, Thomas L. Penner§ & Martin Caffrey*

* Department of Chemistry, The Ohio State University, Columbus, Ohio 43210, USA

† Cornell High Energy Synchrotron Source (CHESS), Cornell University, Ithaca, New York 14853, USA

§ Corporate Research Laboratories, Eastman Kodak Company, Rochester, New York 14650, USA

THE X-ray standing wave (XSW) method, developed in the 1960s, was used originally to determine heavy atom positions in and on silicon and germanium single crystals¹⁻⁷. An X-ray standing wave generated by the interference of coherent incident and reflected beams excites X-ray fluorescence from the heavy atom, the intensity of which as a function of incident angle provides an indication of the atom's distance from the X-ray reflecting surface. The availability of X-ray mirrors and the ability to prepare layered synthetic microstructures has made possible the study of biologically relevant structures using the XSW technique on length scales of typically tens to hundreds of ångströms⁸⁻¹², allowing heavy atoms in such structures to be located with ångström or subångström resolution. Many model biological systems (such as Langmuir-Blodgett films, which mimic membranes) require access to still larger scales, but it is not obvious that an XSW will remain coherent

‡ Present address: Department of Materials Science and Engineering, Northwestern University, Evanston, Illinois 60208 and Argonne National Laboratory, Argonne, Illinois 60439, USA.

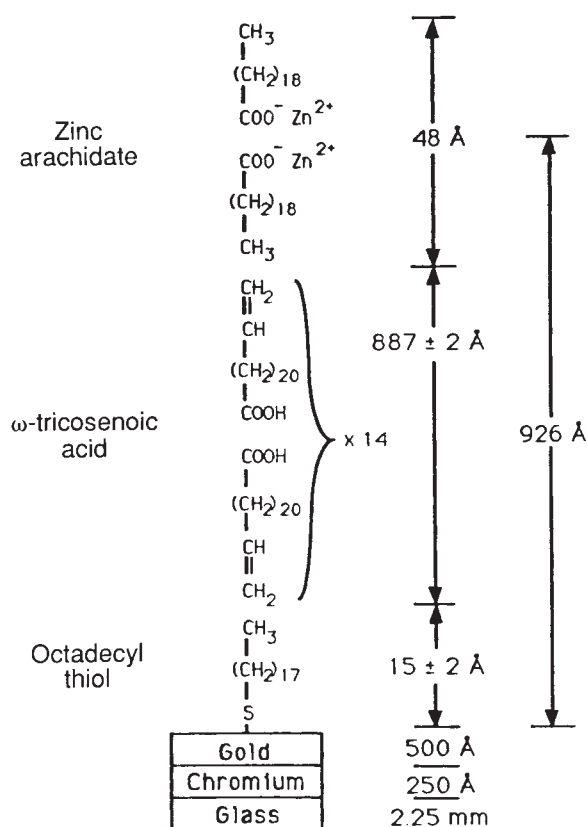


FIG. 1 Schematic of the gold mirror and deposited films. Gold was deposited as a 500-Å-thick film on a piece of chromium-coated float glass (5 cm \times 2.5 cm \times 0.2 cm) using thermoevaporation techniques and was plasma-cleaned before treatment with an octadecylthiol solution. The latter forms a stable, covalently bound monolayer with the hydrocarbon chains at the air-surface interface. Films of ω -tricosenoic acid and zinc arachidate were deposited by the Langmuir-Blodgett method. Transfer ratios were close to unity for each deposition. Film thickness was monitored after each deposition by ellipsometry. The dimensions shown were obtained from ellipsometry in the case of deposited organic films and from the manufacturer's specifications in the case of the mirror.

over such length scales. Here we report studies of a lipid multilayer system using the XSW method, in which we have been able to locate the metal atoms in a zinc arachidate bilayer with ångström resolution at a distance of almost 1,000 Å above the surface of a gold mirror. Our results indicate that the XSW technique should be useful for structural studies of supramolecular aggregates, receptor-ligand interactions and multi-membrane stacks, in which length scales of this order are encountered.

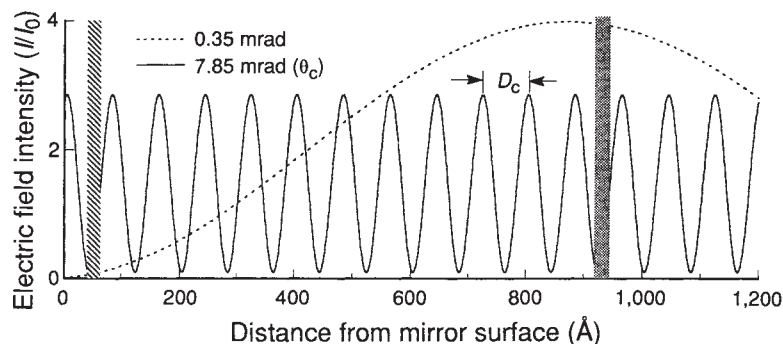
The strategy used to address the nature of the XSW electric field and its usefulness as a long-distance surface probe follows

(see Fig. 1). A hydrophobic gold mirror with 14 bilayers of ω -tricosenoic acid (ω -TA, sample A) and an inverted bilayer of zinc arachidate was prepared which posits the zinc layer between 900 Å and 1,000 Å above the mirror surface. By way of contrast, a second sample (sample B) was prepared that lacked the 14 ω -TA bilayers and had the zinc layer considerably closer to the gold mirror surface. From ellipsometry measurements, we estimated that the zinc layer was \sim 926 Å above the mirror surface for sample A and \sim 42 Å above the surface for sample B.

For this gold mirror system, the coherently related X-ray beams that generate the standing wave correspond to the incident X-ray beam and the beam totally reflected at the mirror surface below its critical angle, θ_c . Total external reflection occurs at the surface of the mirror when the incident angle, θ , is less than θ_c because the refractive index of X-rays is less than unity. We chose to use a gold mirror because the heavier the atoms constituting the mirror surface, the larger is θ_c , which in turn makes data acquisition easier and more accurate. The position of the nodes and antinodes of the standing wave relative to the mirror surface can be calculated for a given X-ray wavelength, λ , and θ , by Fresnel theory^{9,13}. XSW periodicity D is related to θ in the following way: $D = \lambda / (2 \sin \theta)$. Thus, at zero angle when the incident beam and the mirror surface are parallel, the XSW period is infinite in length, and the phase of the standing wave is such that a node coincides with the mirror surface. As θ is increased, the first antinode moves toward the mirror surface and is approximately coincident with the surface when θ reaches θ_c . At the same time the XSW periodicity decreases to $\lambda / (2 \sin \theta_c)$, which corresponds to the 'critical period', D_c . The other nodes and antinodes follow behind the first antinode like a collapsing bellows in the direction of the surface as θ is increased. For the example in Fig. 2, where a heavy-atom layer is situated *in vacuo* at \sim 925 Å above the gold mirror surface, it is apparent that a total of 12 complete XSW antinodes will have traversed the heavy atom layer as θ increases from 0 mrad to θ_c . The photoelectric effect, evidenced by X-ray fluorescence which is maximized whenever the XSW antinode coincides with the midplane of a heavy atom layer, can be used as a probe of the XSW electric field intensity normal to the surface as θ is varied. Conversely, the profile of the fluorescence yield can be used to calculate the position of the electric-field-sensitive heavy atom layer relative to the surface. It is more difficult to make XSW measurements on lighter elements such as oxygen, phosphorus and sulphur, because of their intrinsically weak fluorescence and poor detection efficiency at their characteristically low emission energies.

The results of the XSW measurements are presented in Fig. 3 for the two samples studied. Included in this figure are the experimental fluorescence yield (Fig. 3a and d) and reflectivity profiles (Fig. 3b and e) along with the calculated zinc distribution above the surface (Fig. 3c and f). The theoretical curves were determined by minimizing the χ^2 fit to the data in the region between 3 and 8 mrad. The goodness of fit demonstrates

FIG. 2 The height dependence of the normalized electric field intensity generated during specular reflection of a 9.8-keV (1.265-Å) X-ray plane wave from the surface of a gold mirror. Dashed and solid lines correspond, respectively, to the field profile with the mirror at an angle of 0.35 mrad (0.02°) and 7.85 mrad (0.449°, the critical angle for gold) with respect to the plane of the incident X-ray beam. At low angles, the first antinode of the standing wave is a considerable distance from the surface; at the critical angle, it is next to the surface. The positions of the zinc layers in samples A and B, at 925 Å and 50 Å, respectively, are indicated as shaded rectangles (see text for details). Calculations of electric field intensity, E , are based on Fresnel theory¹³ and assume the following: $E = 9.8$ keV; the mirror is *in vacuo* and the refractive index, n , of the gold film is the same as gold in bulk form ($n = 1 - \delta - i\beta$, where $\delta = 3.08 \times 10^{-5}$ and $\beta = 2.27 \times 10^{-6}$ at the photon energy).



that the XSW is well defined at $\sim 1,000$ Å above the mirror surface and that it can be used to probe structure with dimensions on this same length scale.

The fluorescence yield profile from sample A (Fig. 3a) shows a single monotonically increasing fluorescence intensity from $\theta = 0$ mrad up to the critical angle of the film at $\theta = 2.2$ mrad. This is accounted for by the angle-dependent penetration of the evanescent wave¹⁴⁻¹⁶ through the upper organic-hydrocarbon layer in this region. From the calculations presented above for the idealized case of a zinc layer situated in a vacuum 925 Å above a gold mirror, we find that the first antinode of the XSW formed by the incident beam and that reflected from the gold mirror coincides with the zinc layer when $\theta = 2.3$ mrad. But because the intervening organic layer will, by refraction, bend the incident beam away from the surface normal, the angle of incidence at the gold mirror is now less than that of the incident beam striking the air-film interface and that calculated for the situation *in vacuo*. This effect shifts the fluorescence peaks (and

troughs) to higher nominal angles of incidence. The magnitude of this refractive effect lessens as the nominal incidence angle increases. At $\theta = 7.85$ mrad, however, the angle of incidence at the gold mirror surface below the organic layer is ~ 7.53 mrad. This corresponds to an XSW periodicity of 85 Å in the organic film, in contrast to 80 Å for $\theta = 7.85$ mrad in air. The net effect of the organic layer is thus to reduce the number of fluorescence peaks observed in the $0 < \theta < \theta_c$ region from 12 to 11½. The theoretical curves shown in Fig. 3 take into account these refractive effects.

The decreasing fluorescence beyond the gold θ_c (Fig. 3a and d) is due to the steep drop in the reflected beam intensity in this region (Fig. 3b and e). The mismatch in amplitude between theoretical and experimental low-angle peaks in the fluorescence profile below 3 mrad (Fig. 3a) arises partly from a limited angular resolution in our measurements and partly from an extremely high calculated electric field in this region (see also ref. 17). Experiments are being conducted to test whether

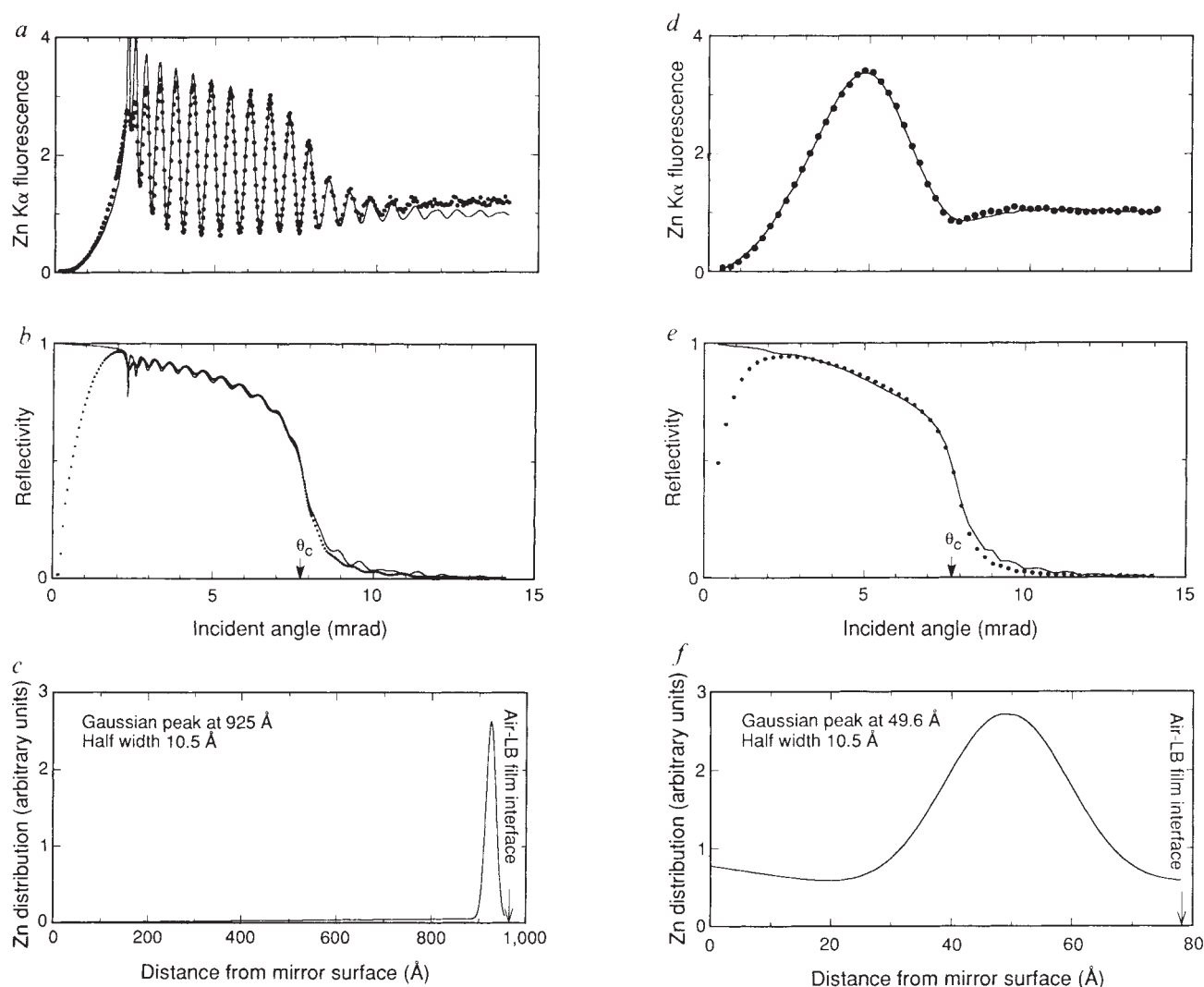


FIG. 3 The experimental (●) and theoretical (—) angular dependence at 9.8 keV of the zinc K α fluorescence yield (a, d) and the specular reflectivity (b, e) for samples with (a, b) and without (d, e) the 14 ω -tricosenoic bilayers. The reflectivity and angle were measured directly on an absolute scale. The fluorescence yields were normalized to the same area of illuminated film at all angles and scaled so that a fluorescence yield of unity is obtained beyond the critical angle. The calculated zinc distribution above the mirror surface is shown for samples with (c) and without (f) ω -tricosenoic acid. The total amount of zinc is normalized to unity. Fluorescence and reflectivity were measured with monochromatic light on the D-line at the Cornell High Energy Synchrotron Source. We used a germanium(111) monochromator to

tune the X-rays to 9.8 keV for optimal excitation of zinc K α fluorescence ($E = 8.9$ keV). Fluorescence data were collected with a Si(Li) solid state detector with an energy resolution of ~ 200 eV. For sample A, zinc K α fluorescence was obtained from a single-channel analyser; for sample B, we recorded complete fluorescence spectra at each incident angle using a multichannel analyser, and we measured the area beneath the zinc K α peak using a χ^2 -minimization gaussian fit and corrected for dead time. Above θ_c , scattering increases and shows up as background in the single-channel analyser data. The data for each point were collected in 3–15 s to ensure 1% counting statistics, with a beam 22 μ m high and 2 mm wide, and the storage ring operating at 5.3 GeV and 35–50 mA total positron current.

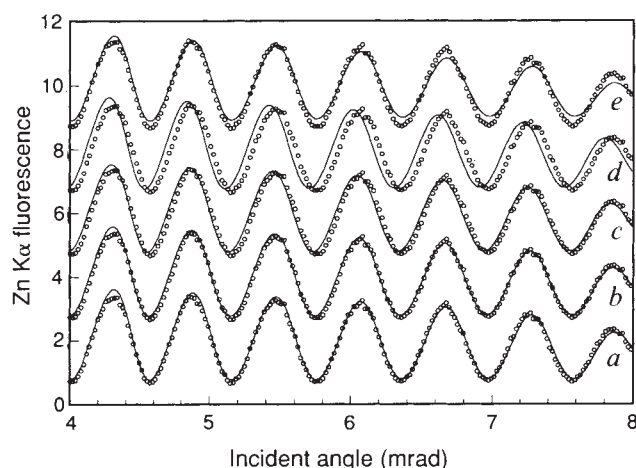


FIG. 4 The sensitivity of the fluorescence yield profile to the mean position of the heavy atom layer above the surface and to the distribution about the mean position is illustrated. The experimental data (●) for zinc K α fluorescence yield were taken from the central position (4–8 mrad) of Fig. 3a. Theoretical curves were generated by assuming a mean zinc position of 925 Å (a), 927 Å (b), 930 Å (c) and 935 Å (d) with a full width at half height of 21 Å. In (e) a mean zinc position of 925 Å and a full width at half height of 31 Å were assumed. Curves are displaced on the ordinate for clarity.

such large fields exist.

The modulation in the reflectivity curve between 2.3 and 7.5 mrad (Fig. 3b) arises from interference between reflections generated at the air-film interface and those generated at the film-mirror interface. An analysis of the reflectivity curve in this region provides an accurate measure of total film thickness (955 ± 5 Å). The reflectivity modulations continue out to higher angles, indeed beyond the point where data were collected in this study. The high-angle modulations contain information useful in reconstructing the electron density profile of the deposited film in the direction of the surface normal. We expect to concentrate on this reflectivity region in future work.

The agreement between experiment and theory is remarkably good as indicated in Fig. 3. This is illustrated more clearly in Fig. 4, which shows how changes in the mean position of the heavy atoms and spread about the mean position affect the goodness of fit. Sensitivity to mean position appears as mismatch in the phase of the modulation, whereas the distribution about the mean position affects the modulation amplitude. These data suggest that the XSW offers extremely good spatial resolution, of the order of several ångströms, on a length scale of just under 1,000 Å.

In conclusion, XSW generated by specular reflection from a gold mirror are well defined at $\sim 1,000$ Å above the mirror surface. The useful probing distance of the element-specific XSW is also of this length scale. At the same time, the spatial resolution of the XSW at such great distances from the surface remains in the range of several ångströms. Thus, variable-period XSW are likely to prove useful in surface structure studies, including membrane-membrane and receptor-ligand interactions, coatings, polymers, organic and inorganic thin films, and a variety of interfacial phenomena. With the advent of brighter X-ray sources and the use of wide-bandpass optics, kinetic studies on such systems will be possible. □

Received 5 August; accepted 11 October 1991.

1. Batterman, B. W. *Phys. Rev. A* **133**, 759–764 (1964).
2. Batterman, B. W. *Phys. Rev. Lett.* **22**, 703–705 (1969).
3. Golovchenko, J. A., Batterman, B. W. & Brown, W. L. *Phys. Rev. B* **10**, 4239–4243 (1974).
4. Andersen, S. K., Golovchenko, J. A. & Mair, G. *Phys. Rev. Lett.* **37**, 1141–1145 (1976).
5. Cowan, P. L., Golovchenko, J. A. & Robbins, M. F. *Phys. Rev. Lett.* **44**, 1680–1683 (1980).
6. Golovchenko, J. A., Patel, J. R., Kaplan, D. R., Cowan, P. L. & Bedzyk, M. J. *Phys. Rev. Lett.* **49**, 560–563 (1982).
7. Bedzyk, M. J. & Materlik, G. *Phys. Rev. B* **31**, 4110–4112 (1985).

8. Bedzyk, M. J., Bilderback, D. H., Bommarito, G. M., Caffrey, M. & Schildkraut, J. S. *Science* **241**, 1788–1791 (1988).
9. Bedzyk, M. J., Bommarito, G. M. & Schildkraut, J. S. *Phys. Rev. Lett.* **62**, 1376–1379 (1989).
10. Bedzyk, M. J., Bommarito, G. M., Caffrey, M. & Penner, T. L. *Science* **248**, 52–56 (1990).
11. Iida, A., Matsushita, T. & Ishikawa, T. *Jap. J. Appl. Phys.* **24**, L675–L678 (1985).
12. Zheludev, S. I., Lagomarsino, S., Novikova, N. N., Kovalchuk, M. V. & Scarinci, F. *Thin Solid Films* **193/194**, 395–400 (1990).
13. Parratt, L. G. *Phys. Rev.* **95**, 359–369 (1954).
14. Marra, W. C., Eisenberger, P. & Cho, A. Y. *J. Appl. Phys.* **50**, 6927–6933 (1979).
15. Becker, R. S., Golovchenko, J. A. & Patel, J. R. *Phys. Rev. Lett.* **50**, 153–156 (1983).
16. Bloch, J. M. et al. *Phys. Rev. Lett.* **54**, 1039–1042 (1985).
17. de Boer, D. K. G. *Phys. Rev. B* **44**, 498–511 (1991).

ACKNOWLEDGEMENTS. This work was supported by a grant from the NIH, a university exploratory research programme award (Procter and Gamble Co) and a DuPont young faculty award to M.C. and by separate grants from Eastman Kodak Company to M.J.B. and M.C. CHESS is supported by the NSF.

The quasiquadrennial oscillation of Jupiter's equatorial stratosphere

Conway B. Leovy*, A. James Friedson† & Glenn S. Orton†

* Department of Atmospheric Sciences, University of Washington, Seattle, Washington 98195, USA

† Jet Propulsion Laboratory, California Institute of Technology, 4800 Oak Grove Drive, Pasadena, California 91109, USA

A NEW 11-year record of Jupiter's stratospheric temperature¹ shows an equatorial temperature oscillation with an apparent period of 4–5 years. Here we compare this oscillation to two long-period oscillations of zonal winds in the Earth's equatorial stratosphere, and propose that the same mechanism—forcing by the stresses of vertically propagating waves—is responsible for the oscillations on both planets. Jupiter's temperature oscillation has been observed for slightly more than two cycles and closely resembles the temperature signatures of the Earth's semiannual oscillation and quasibiennial oscillation. If the mechanisms responsible for these oscillations are indeed similar, Jupiter's oscillation indicates that there is significant vertical momentum transport due to equatorially trapped atmospheric waves, and it may provide a means for probing the poorly understood process of the generation of these waves by convection^{2,3}.

The temperature maxima and minima of the jovian oscillation are centred on the equator, with maxima in 1980, 1984 and 1989–90, and minima in 1982–83 and 1986–87. Figure 1 shows temperature profiles for two pairs of years having opposite phases of the equatorial temperature structure.

Zonal wind oscillations of the quasibiennial oscillation (QBO) have amplitude maxima near 25 mbar (~ 25 km), whereas those of the semiannual oscillation (SAO) are near 1 and 0.02 mbar (45 and 75 km)⁴. Both the QBO and SAO have instantaneous wind profiles in which eastward and westward zonal winds alternate in the vertical. Between zonal wind peaks of opposite sign are wind-shear layers. Time oscillations at a fixed height occur because this profile of alternating winds propagates downwards over time. On Earth, the wind-shear layers are uniquely related to temperature through the geostrophic and hydrostatic relations which together imply that equatorial temperature maxima coincide with positive (eastward) shear layers ($\partial u / \partial z > 0$, where u is eastward zonal wind speed and z is height) and equatorial temperature minima coincide with negative (westward) shear layers ($\partial u / \partial z < 0$) (ref. 5). Jupiter's rapid rotation rate, and the long timescale and zonal alignment of its wind and temperature structure, ensure that its equatorial mean zonal flow is also in geostrophic and hydrostatic balance. Consequently, its equatorial temperature maxima also coincide with positive shear layers, and equatorial temperature minima coincide with negative shear layers.

The Jupiter oscillation resembles the QBO in several respects: (1) long-period oscillation between equatorial shear zones of opposite sign, (2) strong equatorial confinement of the